

## Size-selective trapping and photocatalytic degradation of PFOA in Fe-modified zeolite frameworks

Jan-Max Arana Juve<sup>a,b</sup>, Xavier Baami González<sup>a,c</sup>, Lu Bai<sup>a</sup>, Zhiqun Xie<sup>a</sup>, Yanan Shang<sup>a,d</sup>, Ali Saad<sup>a</sup>, Rafael Gonzalez-Olmos<sup>c</sup>, Michael S. Wong<sup>b</sup>, Mohamed Ateia<sup>b</sup>, Zongsu Wei<sup>a,\*</sup>

<sup>a</sup> Centre for Water Technology (WATEC), Department of Biological and Chemical Engineering, Aarhus University, Ole Worms Alle 3, Aarhus C 8000, Denmark

<sup>b</sup> Department of Chemical and Biomolecular Engineering, Rice University, 6100 Main St, Houston, TX 77005-1827, United States

<sup>c</sup> IQS School of Engineering, Universitat Ramon Llull, Via Augusta 390, Barcelona 08017, Spain

<sup>d</sup> School of Safety and Environmental Engineering, Shandong University of Science and Technology, Qingdao 266590, China

### ARTICLE INFO

#### Keywords:

Zeolite frameworks  
Fe doping  
Size-selective trapping  
Pore opening  
Concentrate-and-degrade

### ABSTRACT

Removal and destruction of perfluorooctanoic acid (PFOA) are challenging due to its extreme persistence and dilute concentrations. This study investigated dual-function adsorptive-photocatalytic zeolite materials to selectively adsorb and degrade PFOA via tuning pore structures and doping transition metals. It is found that the pore opening is critical in the size-selective trapping of PFOA, while the iron doped zeolites present excellent adsorption of PFOA ( $>80 \text{ mg g}^{-1}$ ) combining hydrophobic and electrostatic interactions. The formation of PFOA-iron complexes has reduced bond dissociation energy of C–F, calculated from density functional theory, for favorable stepwise defluorination (over 60% defluorination in 4 hours) by superoxide radicals and ligand-to-metal charge transfer. This mechanistic investigation extends the potential of the concentrate-and-degrade concept to remove PFOA selectively and effectively from contaminated water.

### 1. Introduction

Perfluorooctanoic acid (PFOA) use and release into the environment pose critical risks to human health and ecosystems [1]. In 2023, the United States Environmental Protection Agency (U.S. EPA) proposed a near-zero PFOA national primary regulation (enforcable level of 4 ppt) to limit its presence in drinking water [2]. However, current treatment strategies face the challenges of extremely low PFOA concentrations in  $\text{ng L}^{-1}$  to  $\mu\text{g L}^{-1}$  levels and incomplete defluorination (fluoride released from PFAS molecules as  $\text{F}^-$  ions), which leads to the possible generation of hazardous short-chain perfluoroalkyl carboxylic acids (PFCAs) [3]. Generally, three main strategies are being explored to treat PFOA in laboratory- and large-scale implementations [4]. First, separation technologies such as activated carbon (AC) adsorption, ion exchange resins, and membrane filtration are effective in removing PFOA [5]. However, these technologies result in residual solid or liquid waste that requires further treatments (e.g., regeneration). The second strategy is the use of advanced oxidation/reduction processes based on radical species [6,7] to destroy PFOA molecules, which showed varied levels of treatment efficiency. Particularly a large amount of chemicals is needed

to treat the low-concentration PFOA, which is not sustainable. Third, thermal [8] and hydrothermal [9] decomposition becomes attractive to improve defluorination efficiency but suffers from drawbacks of high cost and extensive energy consumption [10,11].

Therefore, there is an urgent need to find suitable and inexpensive strategies to effectively defluorinate PFOA. In this regard, adsorptive photocatalysts are emerging as possible options [12–15]. For example, a pioneered photocatalyst based on titanate nanotubes loaded on activated carbons (TNT@AC) achieved complete PFOA degradation and approximately 60% defluorination rate. However, doping expensive post-transition metals (e.g., gallium [14] and indium [15]) are often necessary for carbon materials, resulting in low surface area that limits the degradation efficiency. Compared with AC, zeolites with their highly ordered three-dimensional aluminosilicate structure, interconnected void channel, and open pores with defined sizes have distinct advantages. The tunable framework zeolite structure offers more opportunities to improve its capacity to capture PFOA and manipulate the photo-degradation reactions that are hitherto impossible in traditional AC materials [16]. Recently, Qian et al. reported an adsorptive photocatalyst with a commercial Fe-BEA zeolite for both

\* Corresponding author.

E-mail address: [zwei@bce.au.dk](mailto:zwei@bce.au.dk) (Z. Wei).

<https://doi.org/10.1016/j.apcatb.2024.123885>

Received 15 August 2023; Received in revised form 21 February 2024; Accepted 24 February 2024

Available online 26 February 2024

0926-3373/© 2024 The Author(s). Published by Elsevier B.V. This is an open access article under the CC BY license (<http://creativecommons.org/licenses/by/4.0/>).

perfluorooctanesulfonic acid (PFOS) [17] and PFOA [18] degradation, achieving ~40% defluorination rate in 24 hours under UV irradiation. These adsorptive photocatalysts still present unmet needs in PFOA remediation: 1) ineffective adsorption of low-concentration PFOA from the water; 2) low defluorination performance at the catalyst surface after the adsorption step; 3) how the unique structural characteristics of zeolite frameworks (e.g., pore opening, Si/Al composition, and surface properties) impact defluorination reaction; and 4) uncharacterized role of doping species like Fe in the processes of PFOA complexation and reactive species generation.

Provided that pore size is a determining factor for molecule migration and interaction in porous structures [19,20], we hypothesize that tuning the pore characteristics of zeolites comparable to PFOA molecules will enhance the selectivity and effectiveness of PFOA capture. Additionally, this work intends to study the influence of the composition, namely the  $\text{SiO}_2/\text{Al}_2\text{O}_3$  ratio, on PFOA adsorption given the hydrophobic surface resulting from the siloxane structure [21]. Tuning both the pore size and composition may lead to a synergism that enhances the interaction and photodegradation of PFOA at the catalyst surface.

In this work, we selected and tested five zeolites (Mordenite (MOR), Chabazite (CHA), ZSM-5 (MFI), Beta (BEA), and Faujasite (FAU)) with different pore opening but constant  $\text{SiO}_2/\text{Al}_2\text{O}_3$  ratio (~30) to evaluate the effect of pore size on PFOA adsorption. Meanwhile, four different BEA zeolites with different  $\text{SiO}_2/\text{Al}_2\text{O}_3$  ratios were selected to determine the influence of the framework composition and hydrophobicity. Next, Fe-doped zeolites were post-synthesized to promote the photocatalytic activity and the stability of the catalyst. Density functional theory (DFT) calculations were performed to verify the role of doped Fe on the adsorption and photodegradation of PFOA. Our findings provide a systematic analysis of the Fe-doped zeolites as effective, stable, and simple photocatalysts to adsorb and degrade PFOA and potentially other per and polyfluoroalkyl substances (PFAS) [22]. It also opens new horizons to selectively adsorb PFOA molecules in commercial framework materials and achieve high defluorination rates *in situ*.

## 2. Materials and methods

### 2.1. Chemicals and materials

The material composition, textural and structural proprieties, and sources of the commercial zeolites are summarized in Table S1 and Text S1 of the supporting information (SI). PFOA (96%), p-benzoquinone (BZQ) (99%),  $\text{Fe}_2\text{O}_3$  (>99.9%), and ferrous chloride ( $\text{FeCl}_2$ ) (>99%) were purchased from Thermo Scientific. Methanol (99.5%) and potassium iodide (KI) ( $\geq 99\%$ ) were purchased from VWR Chemicals. Isopropanol (ISP) ( $\geq 99.8\%$ ) was purchased from Merck. 5,5-Dimethyl-1-pyrroline N-oxide (DMPO) (>98.0%) for Electron Paramagnetic Resonance (EPR) spectroscopy was purchased from Sigma-Aldrich. Polyether sulfone (PES) filters of 0.22  $\mu\text{m}$  were used to filter all samples prior to analysis.

### 2.2. Fe-doping of commercial zeolites

In a typical procedure, 0.5 g of the selected zeolites were dispersed in 50 mL of 0.1 M Fe salt [23] and shaken for 4 hours in a tumbler at 300 rpm. Next, the resulting slurry was centrifuged at 9000 rpm for 2 minutes and dried at 60 °C overnight. Afterward, the powder was grounded with a mortar and pestle and then calcined at 500 °C for 4 hours (Fig. 1), unless otherwise stated, to prevent the Fe leaching and promote Fe oxidation [24]. The resulting reddish powders were washed with deionized water to remove the remaining saline contents in the material and dried at 60 °C overnight. As a control,  $\text{Fe}_2\text{O}_3$  was used as received and TNT@AC was synthesized as previously reported [12].

### 2.3. Adsorption experiments

Adsorption kinetic tests were carried out with a 10 mL solution of PFOA (1 mg  $\text{L}^{-1}$ ) and 0.01 g of zeolites (1 g  $\text{L}^{-1}$ ), shaken at 200 rpm in the dark. For selected samples, aliquots from the supernatant were taken at predetermined time intervals (*i.e.*, 0, 5, 10, 30, and 60 min), and immediately filtered with a PES filter. The filtrate was then analyzed to determine the concentration of PFOA. Adsorption isotherms were obtained under different PFOA concentrations ranging from 0 to 100 mg  $\text{L}^{-1}$  at 300 rpm agitation for 24 hours.

### 2.4. Photodegradation experiments

Typical photodegradation tests were carried out with 1 g  $\text{L}^{-1}$  of catalyst and 10 mL of 1 mg  $\text{L}^{-1}$  of PFOA. The mg  $\text{L}^{-1}$  level of PFOA concentration was selected to allow accurate tracking of its defluorination and quantification of byproducts. The defluorination efficiency (Eq. 1) is defined as the  $\text{F}^-$  ions released ( $C_{\text{F}^-}$ ) into the solution after the degradation process divided by the total amount of fluorine atoms contained in the initial PFOA concentration ( $C_0$ ):

$$\text{Defluorination}(\%) = \frac{C_{\text{F}^-}}{15 \times C_0} \times 100 \quad (1)$$

The irradiation was carried out in a PCX50C Discover Multichannel Photochemical reaction system (9 channels with one 365 nm UVA lamp each, light intensity of 450  $\text{mW cm}^{-2}$ , and photon flux of  $1.42 \pm 0.08 \mu\text{E} / (\text{L}^{-1} \text{s}^{-1})$ ). The fluence dose was measured by chemical actinometry as previously described [25]. During the photocatalytic process, aliquots were taken at predetermined time intervals (*i.e.*, 10, 30, 60, 120, and 240 min) to analyze the degradation intermediates and defluorination efficiency. PES filters (0.22  $\mu\text{m}$ ) were used to remove the solids in the mixtures. For mass balance analysis, the adsorbed PFOA and its degradation products in the solid phase were extracted via methanol extraction, using 10 mL methanol at 80°C for 4 hours. Later, the mixture was centrifuged and the supernatant was filtered to analyze the PFAS byproducts [12].

The robustness and reusability of Fe-zeolites were examined by reusing the material during 5 consecutive cycles. Material composition stability was evaluated with X-ray photoelectron spectroscopy (XPS),

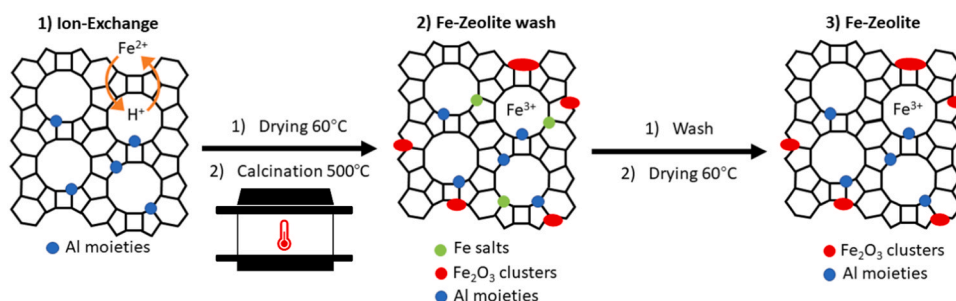


Fig. 1. The scheme of Fe-zeolite synthesis process.

elemental leaching analysis, and calcination tests. The effect of pH was studied by increasing the initial pH range from 2.5 to 11.0. Classical scavenger experiments were conducted to investigate the roles of holes ( $h^+$ ), hydroxyl radicals ( $\cdot\text{OH}$ ), and superoxide ( $\text{O}_2^{\cdot-}$ ) in the photocatalytic degradation of PFOA using 1 mM solutions of KI, ISP, and BZQ, respectively [12]. EPR (Bruker Magnetech ESR5000) was also used to verify the formation of radical species using 80  $\mu\text{L}$  of  $\text{H}_2\text{O}$  and 50  $\mu\text{L}$  of 100 mM of 5, 5-dimethyl-1-pyrroline N-oxide (DMPO) in methanol as  $\cdot\text{OH}$  trapping agent prior irradiation [26]. The frequency was fixed at 9.45 GHz, the microwave power was 35 mW, and the temperature was 33  $^\circ\text{C}$ .

## 2.5. Characterization methods

The particle morphology was imaged using a Scanning Electron Microscope (SEM; Nano NOVA), while the elemental screening was analyzed with energy-dispersive X-ray spectroscopy (EDS) (TM3030Plus Tabletop). The average particle size was estimated with the software ImageJ, by averaging the maximum and minimum length of 10 randomly selected particles in the SEM images. A Transmission Electron Microscope (TEM; JEM-2100 F) was used for high-resolution imaging, structural characterization, and local compositional analysis of the catalyst surface. The lattice spacing in TEM images was measured in ImageJ software. The zeta potential of the materials was measured with a zeta potential analyzer (Malvern Zetasizer Nanoseries ZS). The crystalline structures were analyzed by a Bruker X-ray diffractometer (XRD; Rigaku SmartLab) equipped with Cu  $K\alpha$  radiation ( $\lambda = 1.5418 \text{ \AA}$ ) and at a scanning rate ( $2\theta$ ) of  $2^\circ \text{ min}^{-1}$ . The surface chemical compositions, along with oxidation states, were analyzed with a Phi Quantera X-ray photoelectron spectroscopy (XPS) (15 kV and 15 mA (Al  $K\alpha$  X-ray)) using the standard C 1 s peak (Binding energy,  $E_b = 284 \text{ eV}$ ) for calibration and elimination of static charge effects. Fourier-transform infrared spectroscopy (FTIR; Vertex 70 V) tests were performed to evaluate the variations in the surface functional groups at different calcination temperatures and to confirm the typical BEA functional groups in the different composition samples. The light absorption was evaluated to determine the responsive spectrum using a UV/Vis Spectrophotometer (Thermo Scientific, Genesys 150). The cyclic voltammetry of the photocatalysts was evaluated with an Electrochemical Analyzer (CH Instruments; CHI760E), using 50 mL of a 0.5 M  $\text{Na}_2\text{SO}_4$  electrolyte solution, to evaluate the electrical charge storage capacity, or the oxygen adsorption capacity, of the materials. The specific surface area and pore size distribution are properties affecting the adsorption of the materials, which were measured by a Brunauer–Emmett–Teller (BET; Quantachrome Autosorb iQ3) analyzer. The Al coordination modes of the materials are determined by the acid sites, which were measured with a chemisorption analyzer (Micromeritics Autochem II RS232) using ammonia gas.

## 2.6. Analytical methods

High-concentration PFOA in adsorption isotherm tests was analyzed using a 1260 Infinity II Agilent high-performance liquid chromatography (HPLC) with a diode array detector (Text S2A), as previously reported [25,27].  $\text{F}^-$  ions in the aqueous phase were analyzed and quantitatively determined using an ion chromatography (IC) system (Dionex Aquion, Thermo Scientific) with an IonPac AS23 column (detailed methods described in Text S2A). Aqueous PFOA and its degradation intermediates were analyzed through ultra-high-performance liquid chromatography coupled with a triple quadrupole mass spectrometer (UHPLC-MS/MS, TSQ Fortis Plus, Thermo Scientific). Concerning the leaching of metals, the amount of the dissolved Fe in the sample supernatant after the photodegradation experiments was measured with an inductively coupled plasma-optical emission spectroscopy (ICP-OES) (OPTIMA 4300 DV, Perkin Elmer). The Fe content of the Fe-doped BEA sample with a  $\text{SiO}_2/\text{Al}_2\text{O}_3$  ratio of

150 was verified via sample digestion and ICP analysis (Text S2B).

## 2.7. DFT calculations

Theoretical calculations were performed to describe the adsorption mechanism of PFOA onto the Fe sites of the Fe-BEA zeolite and estimate the potential change of the decarboxylation energy subject to complexation with Fe species. Geometry optimization was carried out at the B3LYP/6–31 G(d) level theory using Gaussian 09 software [28]. The single point energy of the optimized configurations for neutral Fe-zeolite ( $E_{\text{Fe-zeolite}}$ ), PFOA anion ( $E_{\text{PFOA}}$ ), and Fe-zeolite-PFOA ( $E_{\text{total}}$ ) was then calculated at the B3LYP/6–311 G(d,p) level theory. The adsorption energies ( $E_{\text{ads}}$ ) were calculated to evaluate the interaction between the Fe-zeolite and PFOA (Eq. 2).

$$E_{\text{ads}} = E_{\text{total}} - E_{\text{Fe-zeolite}} - E_{\text{PFOA}} \quad (2)$$

The electrostatic potential (ESP) isosurface diagrams were drawn and rendered with Multiwfn [29] and Visual Molecular Dynamics [30]. Then, the C–C bond dissociation energies (BDE) in the PFOA anion structure (carboxylate anion for carboxylic acids) were calculated using Eq. 3:

$$\text{BDE} = \left( E_{\text{radical}[\text{fragment}1]}^* + E_{\text{radical}[\text{fragment}2]}^* \right) - E_{\text{parent PFOA}} \quad (3)$$

where  $E_{\text{radical}[\text{fragment}]}^*$  represents the single point energy of the related configuration of the fragment and  $E_{\text{parent PFOA}}$  represents the complete configuration [31].

## 3. Results and discussion

### 3.1. Zeolite properties and post-synthesis modification

The zeolite morphology, crystallography, and composition were studied for the different frameworks. SEM images (Figure S1) of the zeolites form aggregates of hundreds of nanometers. Specifically, MOR, BEA, and FAU present a regular cubic shape with homogeneous particle sizes (Figure S2A). CHA is in similar shape with higher size variability and MFI zeolites exhibit rectangular morphologies in octagonal shape. The size distribution (Figure S2 B-G) reveals that the zeolites present normal distributions, except for MFI which presents a positive skew given the variability in the length of the particles. BEA zeolites with  $\text{SiO}_2/\text{Al}_2\text{O}_3$  ratios from 30 to 500 (i.e., BEA30, BEA150, BEA360, and BEA500) also present cubic-like morphology particles with round edges (Figure S3). While the XRD diffractograms confirm BEA compositions (Figure S4A-B; see discussion in Text S3), the surface functional groups of the zeolites are analyzed by FTIR spectrometry (Figure S4C-D). The bands at 1095 and 1220  $\text{cm}^{-1}$  for calcined BEA zeolites are attributed to asymmetric stretching vibrations of the Si–O–Si bond [32] and the band at 820  $\text{cm}^{-1}$  corresponds to the symmetric stretching vibration of the Si–O–Si bond [32,33].

The BET analysis of all zeolites present Type I isotherms (Figure S5A–B), i.e., the characteristic of microporous materials. The pore size of the zeolite frameworks ranges from  $<7.2 \text{ \AA}$  to  $10.8 \text{ \AA}$  without direct correlation with their pore opening size (Fig. 2A). In comparison, the surface areas of BEA ( $1751 \text{ m}^2 \text{ g}^{-1}$ ) and FAU ( $855 \text{ m}^2 \text{ g}^{-1}$ ) are among the highest (Fig. 2A). Likewise, it seems the surface area of BEA30 ( $1751 \text{ m}^2 \text{ g}^{-1}$ ) and BEA150 ( $1925 \text{ m}^2 \text{ g}^{-1}$ ) with low  $\text{SiO}_2/\text{Al}_2\text{O}_3$  ratios present higher surface area than BEA360 ( $340 \text{ m}^2 \text{ g}^{-1}$ ) and BEA500 ( $671 \text{ m}^2 \text{ g}^{-1}$ ) (Figure S5C). BEA30 and BEA150 also exhibit higher surface area than other zeolites. Noted, the surface area is often determined by synthesis parameters (e.g., composition, seeding, templates, temperature) [34,75], and further investigation on the synthesis parameters are encouraged to improve PFAS treatments. With Fe-doping, a negligible change in the surface area is observed for BEA150 (1925 to  $1905 \text{ m}^2 \text{ g}^{-1}$ ).

Since  $\text{Al}^{3+}$  coordinated with oxygen to form octahedral  $\text{AlO}_4^-$

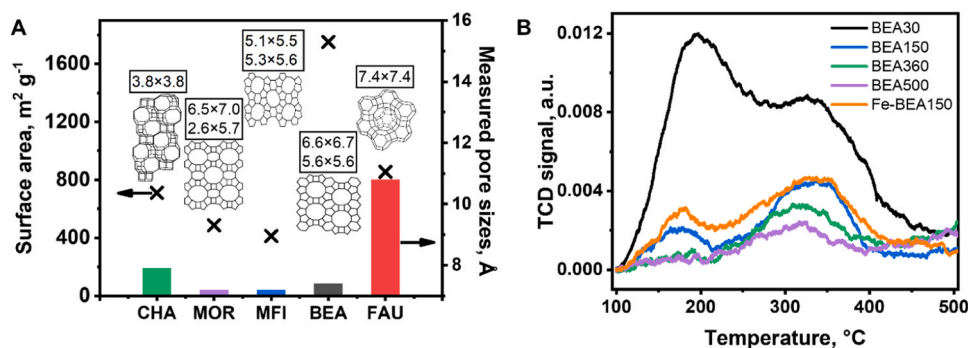


**Fig. 2.** A) Measured surface area (left Y axis), pore size (right Y axis), and reported pore openings in  $\text{\AA}$  (boxes) [35] for different zeolite structures ( $SiO_2/Al_2O_3$  ratio  $\sim 30$ ); B) Temperature programmed desorption for acid sites measured based on the thermal conductivity detector (TCD) signal. Two ammonia desorption temperatures are observed: the weakly bonded ammonia ( $\sim 175^{\circ}C$ ) corresponds to H-bonded physisorbed ammonia molecules while the higher temperatures ( $\sim 325^{\circ}C$ ) correspond to chemisorbed  $NH_3$  corresponding to the extra framework aluminum [36,37].

moieties, which can protonate to form a Brønsted acid site,  $Fe^{3+}$  can be adsorbed onto the framework and exchanged with the  $H^+$ . In addition, tetrahedral extraframework aluminum can be partially bonded to form Lewis acid sites [38,39]. As expected, temperature-programmed desorption (TPD) (Fig. 2B) confirmed the decrease of acid sites when the  $SiO_2/Al_2O_3$  ratio increases (Figure S5D). Fe-doping is essential for the zeolite to present photoactive properties, and Fe could slightly increase the number of acid sites for BEA150 (Figure S5D). The incorporation of Fe into the selected zeolites was confirmed by the EDS analysis (Figure S6A-B and Table S2), which shows and quantifies the presence of Al, Si, and O elements in addition to Fe. The elemental semi-quantitative compositional analysis of the Fe-doped samples confirmed the reported  $SiO_2/Al_2O_3$  ratios ( $30.8 \pm 3.7$ ) (Table S2). Although the doped Fe could not be identified by XRD studies due to its low content and highly uniform distribution [40], the color change from white to reddish after doping suggests the transition of the adsorbed Fe from a lower state ( $Fe^{2+}$ ) to a higher state ( $Fe^{3+}$ ) (Figure S7A). Additionally, the XRD pattern of calcinated  $FeCl_2$  salt (Figure S7B) also confirmed the

formation of  $\alpha-Fe_2O_3$  due to the presence of peaks corresponding to crystalline iron oxide [41] and the particle size distribution analysis revealed slightly larger particles after Fe doping, attributed to surface  $\alpha-Fe_2O_3$  clusters (Figure S2E and S2G). The digestion of Fe-BEA zeolite ( $SiO_2/Al_2O_3$  ratio=150) and subsequent ICP analysis quantified the weight percentages of Fe in the zeolite sample, resulting in a  $1.48 \pm 0.01$  doping percentage. The elemental Si and Al weight percentages, estimated from the ICP tests, were about 35.8% and 0.4%, respectively.

### 3.2. Performance and stability of the materials

#### 3.2.1. Adsorption performance

The adsorption capacity of the zeolite frameworks was first evaluated. As shown in Fig. 3A, BEA and FAU with higher surface areas presented superior adsorption compared to MOR, CHA, and MFI. To normalize the adsorption capacity, the PFOA surface coverage was calculated from the ratio of the maximum adsorbed PFOA amount over the material surface area. The surface coverage increases in general with

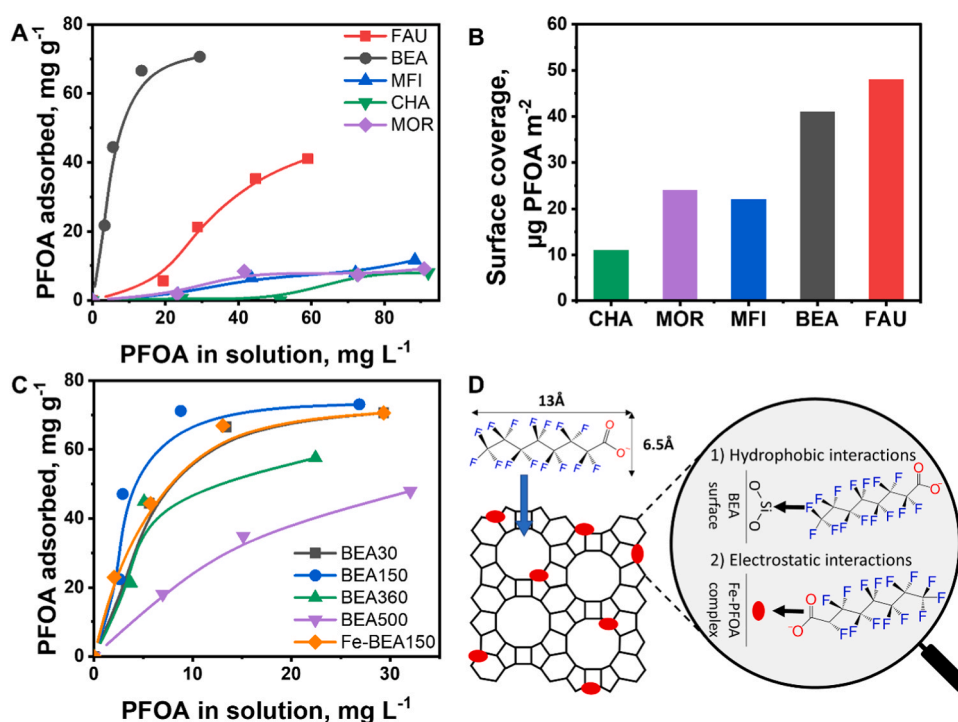


**Fig. 3.** A) PFOA adsorption isotherms; B) PFOA surface coverage on zeolite frameworks; C) Influence of the  $SiO_2/Al_2O_3$  ratio on the PFOA adsorption isotherms; D) Hydrophobic interaction between PFOA tail and Si, as well as electrostatic interaction between negatively charged PFOA head and Fe sites on the zeolite surface.

the pore opening: CHA ( $3.8 \times 3.8 \text{ \AA}$ ) < MOR ( $2.6 \times 5.7 \text{ \AA}$ ) ~ MFI ( $5.1 \times 5.5 \text{ \AA}$ ) < BEA ( $6.6 \times 6.7 \text{ \AA}$ ) < FAU ( $7.4 \times 7.4 \text{ \AA}$ ) (Fig. 3B).

Given the estimated size of a PFOA molecule as  $13 \text{ \AA} \times 6.5 \text{ \AA} \times 6.5 \text{ \AA}$  [42], its diameter matches the best with the pore opening size of BEA ( $6.6 \times 6.7 \text{ \AA}$ ) and FAU ( $7.4 \times 7.4 \text{ \AA}$ ). The highest PFOA adsorption by BEA and FAU supported the hypothesis that the PFOA adsorption is size-selective to access the zeolite pore, and a comparable pore opening size is favorable to the molecule migration. Comparatively, the small pore opening ( $3.8 \times 3.8 \text{ \AA}$ ) and folded 3D-interconnected structure of CHA inhibited the PFOA adsorption. Similarly, the small MFI opening ( $5.1 \times 5.5 \text{ \AA}$ ) also limited the PFOA adsorption. MOR zeolite consisting of 12-rings ( $7.0 \times 6.5 \text{ \AA}$ ), although interconnected with limiting 8-rings ( $2.6 \times 5.7 \text{ \AA}$ ), can still allow PFOA to pass, yet its small interconnected pore size (below the detection limit,  $< 7.2 \text{ \AA}$ ) prevents further molecular diffusion and limits higher adsorption. In contrast, FAU and BEA zeolites exhibit detectable average pore size values of  $10.8 \text{ \AA}$  and  $7.4 \text{ \AA}$ , respectively, which is not the limiting factor for PFOA capture. Therefore, it seems the size exclusion effect prevails in the adsorption of PFOA, while pore size still plays a role after PFOA migrates into the porous

structure.

Furthermore, the surface potentials of BEA and FAU are less negative compared to the other zeolites (Figure S7C), which decreases the electrostatic repulsion between the zeolites and PFOA anions at near-neutral pH conditions. Since electrostatic interactions can be excluded, hydrophobic interactions originating from the siloxane bond [21] play a major role in the PFOA adsorption on commercial zeolites. We hence studied the effect of the BEA composition, *i.e.*, increasing  $\text{SiO}_2/\text{Al}_2\text{O}_3$  ratios, on PFOA adsorption (Fig. 3C). While the relatively small surface areas of BEA360 and BEA500 (Figure S5C) result in low PFOA adsorption, the observation of higher PFOA uptake by BEA30 and BEA150 confers hydrophobic interaction between F and Si. The Langmuir (Table S3) and Freundlich (Table S4) adsorption models (detailed in Text S4) were used to study the adsorption properties of the materials. The adsorption data presented better fitting with the Langmuir model [43], suggesting homogeneous zeolite surface properties (Text S4). The highest PFOA adsorption capacity ( $> 80 \text{ mg g}^{-1}$ ) for BEA150 and BEA30 is comparable to that of GAC materials ( $112\text{--}161 \text{ mg g}^{-1}$ ) [44] and TNT@AC materials ( $> 80 \text{ mg g}^{-1}$ ) [12]. However, the adsorption rate for BEA150 was 59%

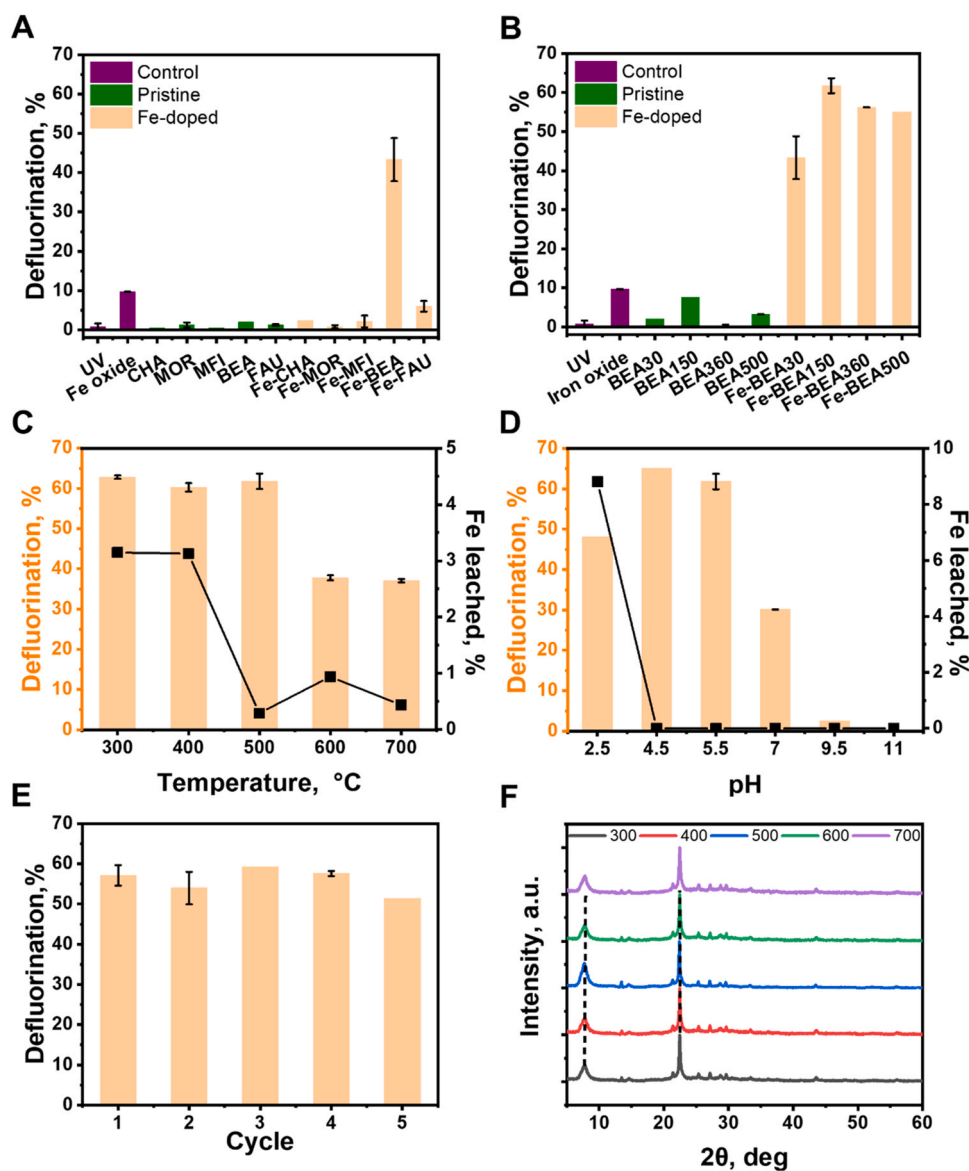


Fig. 4. Defluorination of PFOA by A) different zeolite frameworks and B) zeolite BEA with different  $\text{SiO}_2/\text{Al}_2\text{O}_3$  compositions; Defluorination and Fe-leaching at different C) calcination temperature and D) pH by Fe-BEA 150; E) Reusability of Fe-BEA 150; F) XRD diffractogram of Fe-BEA 150 marked BEA characteristic peaks at  $7.7$  and  $22.5^\circ$  [52] at different calcination temperatures ( $300\text{--}700^\circ\text{C}$ ).

higher than BEA30 as shown in Fig. 3C. Given their comparable surface areas, the faster adsorption for BEA150 confirms the importance of the hydrophobicity of the Si composition in PFOA adsorption.

Although the alumina content increases the negative charge of the structure by populating the Al acid sites, the negative surface charge may be compensated by a cation (e.g.,  $\text{Fe}^{3+}$ ) [45–47]. Therefore, besides the hydrophobic interactions with the zeolite structure, additional “local” electrostatic interactions with the Fe-doped species could also complex negatively charged PFOA ( $\text{pK}_a < 2.8$  [48]) at tested pH (Fig. 3D). However, a slight decrease in PFOA adsorption was observed for Fe-BEA150 compared to pristine BEA150, probably due to a decrease in the average pore size observed near the detection limit (Figure S7D). It should be noted that the pore blocking by the surface-doped Fe species does not result in a significant surface area decrease (Figure S5C).

### 3.2.2. Degradation performance

In the first stage, the defluorination tests by the selected zeolites before and after iron doping were performed, as displayed in Fig. 4A. Although the defluorination efficiency slightly improved after the incorporation of iron, it is still lower than 10% except for the Fe-doped BEA zeolites. Fe-BEA30 reached above 40% defluorination confirming the importance of Fe-doping, comparable pore adjustment, and high surface area for PFOA adsorption and degradation. However, the catalyst cannot achieve complete defluorination after 24 hours, likely due to the formation of short-chain byproducts (Figure S8A). Despite FAU effectively adsorbed PFOA (Fig. 3B), the negligible defluorination efficiency of Fe-FAU compared to Fe-BEA indicates the constrained unique porous structure of zeolite BEA for PFOA selective degradation.

In the second stage, the defluorination of PFOA was evaluated by the Fe-BEA zeolites with different  $\text{SiO}_2/\text{Al}_2\text{O}_3$  ratios (Fig. 4B). In contrast to pristine zeolites, all Fe-doped zeolites exhibited remarkable defluorination efficiencies (>40%), and Fe-BEA150 outperformed all of them reaching ~60% defluorination. As shown in Figure S8B, Fe-BEA150 yields the lowest percentage of short-chain byproducts together with the highest  $\text{F}^-$  ion concentration after 4 hours of treatment (Figure S8C). The PFOA degradation yields more persistent short-chain PFCA byproducts that are also more hydrophilic resulting in less interaction with the zeolite surface. This decreased the possibility of approaching to the active sites on the catalyst surface. It seems the adsorption of PFOA towards Fe-BEA150 is the key to maximize PFOA defluorination. Besides, the chemical actinometry experiments permit the determination of the fluence dose (Figure S8C) and the minimum power required to treat a given volume in the reaction conditions using the photon flux calculated [25]. Given the importance of defluorination to prevent byproduct formation and the challenges to achieve complete defluorination [49], we calculated the minimum amount of energy required to release half of the organic fluoride contained in the initial PFOA solution, resulting in  $27.9 \text{ kWh m}^{-3}$  for our system.

The performance of Fe-BEA150 was then evaluated under different calcination temperatures and solution pH. Upon calcination,  $\text{Fe}_3\text{O}_4$  is the stable phase at  $300^\circ\text{C}$ , while  $\text{Fe}_2\text{O}_3$  is present at  $500$  and  $700^\circ\text{C}$  [24, 50]. The Fe-BEA150 calcinated at low temperatures ( $300$ – $500^\circ\text{C}$ ) presents high defluorination rates (Figure S8D), but only the calcination treatment under  $500^\circ\text{C}$  significantly reduced the Fe leaching (Fig. 4C). Therefore,  $500^\circ\text{C}$  was selected as the optimal calcination temperature for stable catalyst production, as confirmed by XPS analysis after adsorption and photodegradation (Figure S9A–D). Fig. 4D shows the impact of solution pH ( $2.5$ – $11$ ) on PFOA defluorination by the Fe-BEA150 catalyst. An exception occurs at pH 2.5 where the acidic environment threatens the stability and reusability of the catalyst resulting in a lower defluorination rate and high Fe leaching. Higher pH promotes the stability of  $\text{Fe}_2\text{O}_3$ , which has a point of zero charge (PZC) of 6.7 [12]. Although the surface charge of the overall material remains negative (Figure S10A), the presence of iron oxide can locally attract the carboxylate head of PFOA through electrostatic interactions at near-neutral and acidic pH. Therefore, the optimum PFOA degradation

was observed at pH 4.5. At higher pH ( $9.5$ – $11$ ), the particle surface becomes even more negatively charged and repels the PFOA anions, leading to decreased defluorination rates. In addition, at alkaline pH (e.g., 11) the hydroxyl ion can attack the deprotonated  $[\text{Al-O-Si}]^-$  moiety to partially or completely destroy the pristine structure [51] and thus inhibit the defluorination as observed.

### 3.2.3. Reusability and stabilization

The reusability test (Fig. 4E) showed that the catalytic activity maintained around 55% defluorination of PFAS and negligible leaching of the doped Fe (below 2%) was monitored after every cycle. Moreover, it is necessary to reveal the importance of the calcination step on the catalyst stability. In Figure S10B, no obvious difference was observed between the calcined and non-calcined Fe-BEA150 samples. However, the calcination step has significantly reduced the Fe leaching (Figure S10C), stabilizing Fe-modified zeolite and fulfilling the discharge requirements to avoid secondary contamination and additional treatments [53]. However, methanol extraction confirmed that about 8% of the fluoride fraction was found to be adsorbed onto the material as PFCAs after 4 hours (Figure S10D). It demonstrates the importance of subsequent treatments to remove PFAS residuals when reusing the catalyst. The XRD diffractograms show no change in the zeolite BEA phase diffraction peaks at different calcination temperatures (Fig. 4F) and the functionalities of the material do not alter the zeolite crystalline structure with the increase of the calcination temperature, as confirmed by the FTIR analysis in Figure S11A. This suggests both a stable performance and material composition during the synthesis and PFOA degradation experiments.

## 3.3. Mechanistic insights

### 3.3.1. Adsorption mechanism

The PFOA adsorption onto the BEA zeolites is confirmed by FTIR spectroscopy (Figure S11B). C–F stretching vibration is observed at  $1200 \text{ cm}^{-1}$ , which is absent in the zeolite sample before adsorption tests [54]. The absence of the Si–F bond suggests that the adsorption is either attributed to hydrophobic interactions with the zeolite surface or electrostatic interactions with the local positively charged  $\text{Fe}_2\text{O}_3$  sites, not directly forming covalent bonds [55].

The oxidation state of the incorporated iron in Fe-BEA was evaluated by XPS spectra. The deconvolution of the high-resolution XPS of Fe 2p (Fig. 5A) reveals the presence of Fe  $2p_{3/2}$  ( $711.1 \text{ eV}$ ), Fe  $2p_{3/2}$  satellite ( $718.3 \text{ eV}$ ), and Fe  $2p_{1/2}$  peaks ( $724.3 \text{ eV}$ ). The peaks positioned at  $709.7$  and  $712.4 \text{ eV}$  are in agreement with the reported values for  $\text{Fe}^{3+}$  [56]. The presence of a  $\text{Fe}^{3+}$  and the lack of satellite  $\text{Fe}^{2+}$  [57] confirm the major  $\text{Fe}^{2+}$  oxidation upon calcination. Meanwhile, TEM imaging of the Fe-BEA150 (Fig. 5B) also elucidates the presence of dark clusters at the surface of the material (Fig. 5B, blue mark) and in the inner zeolite structure (Fig. 5B, yellow mark). The dark regions present higher Fe content (Figure S12A) compared to brighter areas (Figure S12B) of the material. Besides, the lattice spacing of the Fe-rich region (Figure S13 A–B) is  $0.3 \text{ nm}$ , which corresponds to the plane (2 2 0) of  $\text{Fe}_2\text{O}_3$  [58]. Similar observations were reported for  $\text{Fe}_2\text{O}_3$  clusters onto FAU zeolites [59]. As expected, bright areas in Fe-BEA150 present lattice spacing of  $1.1 \text{ nm}$  (Figure S13 C–D), which is similar to the previously reported for BEA zeolites [58].

The successful local doping of Fe species is reported to adsorb PFOA in a mono or bidentate mode on the  $\alpha\text{-Fe}_2\text{O}_3$  clusters [12]. Further, FTIR tests (Figure S14A) suggest the decreased distance of the carboxylate signals of PFOA from  $242$  to  $228 \text{ cm}^{-1}$  compared to the adsorbed sample [60,61], which results in a bidentate mode complexation facilitating the decarboxylation. We hence used DFT calculations to verify the favorable adsorption mechanism, revealed by the electrostatic potential mapping (Fig. 5C–E) of the Fe-doped zeolite, PFOA, and complexation of PFOA with Fe-zeolite. The negatively charged nucleophilic head of PFOA (blue region in Fig. 5C) can preferentially be adsorbed onto the Fe moieties of

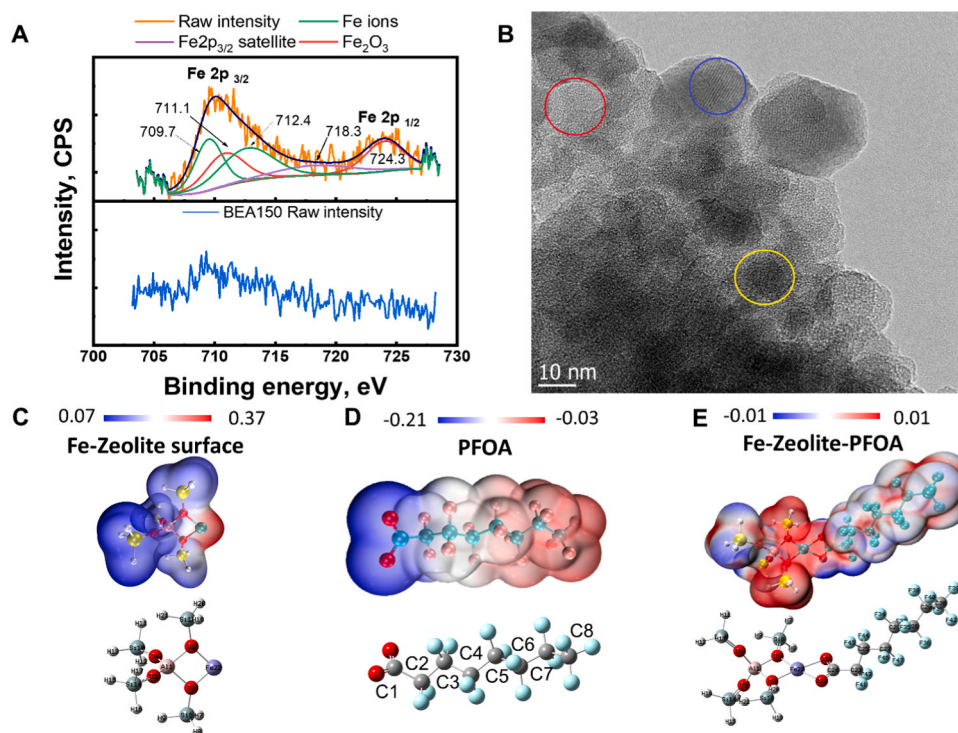


**Fig. 5.** A) Fe2p High-resolution XPS of BEA150 and Fe-doped BEA150 zeolites; B) TEM image of Fe-BEA150 zeolites (red, blue, and yellow circles correspond to areas with the zeolite structure, the external and the internal  $\text{Fe}_2\text{O}_3$  clusters, respectively); Electrostatic potential mapping and adsorption orientation of C) Fe-BEA zeolite, D) PFOA, and E) Fe-zeolite with adsorbed PFOA. In the electrostatic potential map, the blue regions present negative molecular electrostatic potential, the red regions correspond to positively charged potential, and the white correspond to neutrally charged regions. The represented elements in the structures are H (white), Fe (blue), O (red), Al (light red), Si (dark grey), and F (light blue).

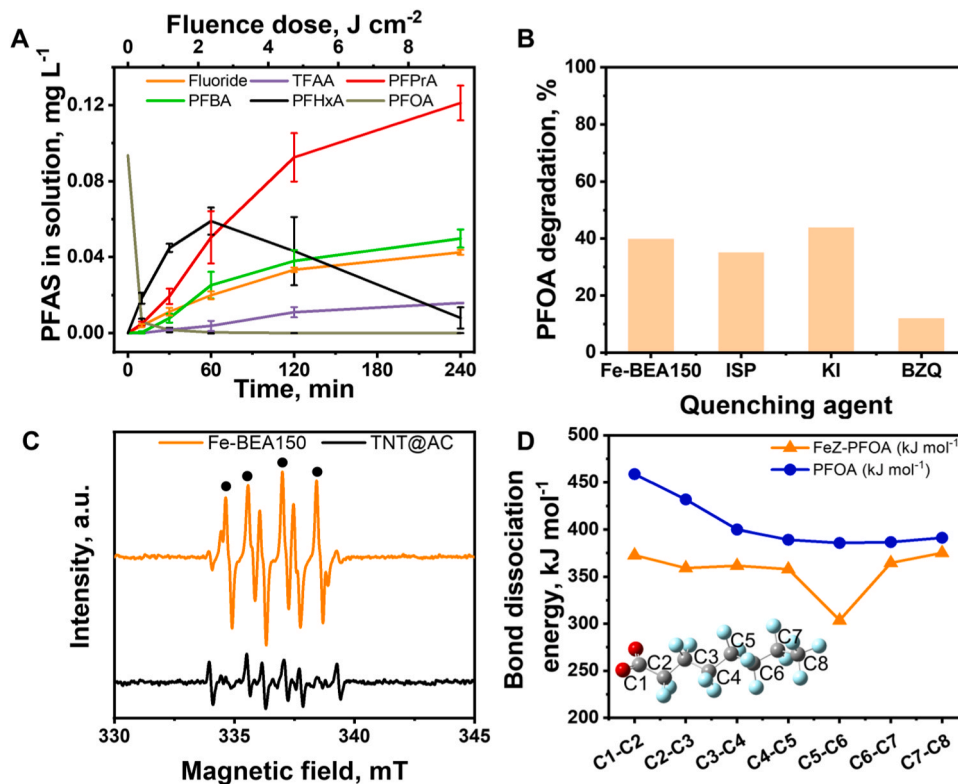


**Fig. 6.** A) Speciation of PFOA and its degradation intermediates in the reaction solution (stirring speed = 300 rpm; PFOA concentration =  $1 \text{ mg L}^{-1}$ ; catalyst dose =  $1 \text{ g L}^{-1}$ ); B) Quenching tests in Fe-BEA150 photodegradation (reaction time = 10 minutes, quenching agent concentration = 1 mM); C) EPR tests for Fe-BEA150 and TNT@AC. The solid circle corresponds to the main spin adducts ( $\text{DMPO-O}_2^-$ ) resulting from trapping  $\text{O}_2^-$  [66]; D) Bond dissociation energy of the  $\text{C}_n\text{-C}_{n+1}$  bond of PFOA anion in solution and adsorbed onto the Fe-BEA zeolite.

the material (red region in Fig. 5D). The resulting PFOA adsorption energy of the optimized system (Fig. 5E) is  $-7.219$  eV, which supports the spontaneous PFOA complexation [13] and may favor subsequent photodegradation. Additionally, the Fe-doping led to a slight increase in PFOA adsorption (Table S3) of BEA150 from  $83.4$   $\text{mg g}^{-1}$  to  $89.1$   $\text{mg g}^{-1}$ , despite the slightly decreased surface area from  $1925$  to  $1905$   $\text{m}^2 \text{g}^{-1}$  (Figure S4C). These results support the electrostatic attractions between the doped  $\text{Fe}_2\text{O}_3$  and PFOA, which allow Fe-BEA150 to maintain fast PFOA adsorption, i.e.,  $>99\%$  removal within 5 min (Figure S14B). In addition, the PFOA adsorption by  $\text{Fe}_2\text{O}_3$  was significantly lower, compared with the zeolite frameworks. In summary, suitable pore openings are critical for PFOA to migrate into the porous structure of zeolites where the surface Si composition drives the hydrophobic interactions with the migrating PFOA and doped  $\text{Fe}_2\text{O}_3$  contributes to electrostatic interactions.

### 3.3.2. Photodegradation mechanism

The Fe-zeolite is capable of initiating the PFOA degradation via Fe complexation and ligand-to-metal charge transfer [18]. Fig. 6A shows a gradual increase in the defluorination rate (orange line) and the accumulation of PFOA degradation intermediates in the reaction solution. Particularly, perfluorohexanoic acid (PFHxA – black line;  $\text{C}_6$ ) rapidly increased at the beginning and started decreasing after 60 minutes attributed to the photocatalytic decomposition. As a comparison, perfluorobutanoic acid (PFBA;  $\text{C}_4$ ), perfluoropropionic acid (PFPrA;  $\text{C}_3$ ), and trifluoroacetic acid (TFAA;  $\text{C}_2$ ) continued to increase. In line with these results, the removal of individual PFCAs by Fe-BEA zeolites demonstrates the preferential removal of PFOA over shorter-chain PFCAs (Figure S15A). PFOA removal is complete after 4 hours of irradiation, while PFBA and PFPrA removal remain modest (below 20%). Similarly, PFOA defluorination is over 20% higher compared to PFBA and PFPrA. Further studies combining different zeolite frameworks may offer a path for size-selective removal of a broader range of PFAS molecules.

To elucidate the PFOA photodegradation mechanisms, classical quenching experiments were performed to identify the effective reactive species in the Fe-BEA150 system. BZQ, KI, and ISP were selected as scavengers for  $\text{O}_2^{\bullet-}$ ,  $h^+$ , and  $\bullet\text{OH}$ , respectively. Fig. 6B shows that BZQ greatly inhibited PFOA degradation. Increasing the BZQ concentration from 0.1 to 1 mM resulted in up to  $\sim 40\%$  inhibition (Figure S15B), suggesting that  $\text{O}_2^{\bullet-}$  can play a role in the degradation process as  $\text{Fe}^{2+}$  oxidant, reaction initiator, or a supporting degradation agent. The  $\text{Fe}^{2+}$  oxidation has already been reported under slightly acidic conditions via superoxide or molecular oxygen (Eqs. 4–7) [62].



In addition, a slight decrease was observed in the presence of ISP suggesting a minor or negligible contribution from  $\bullet\text{OH}$ . No effect was observed for KI, which confirms that  $h^+$  did not play a role in PFOA degradation. These results suggest that superoxide might contribute to the reaction upon UV irradiation. Recent works report thermodynamically favored superoxide reactions with PFCAs due to the low energy barrier for electron capture via superoxide ( $24.78$   $\text{kcal mol}^{-1}$ ) for decarboxylation and defluorination [63]. Similarly,  $\text{S}_\text{N}2$  reactions are also favorable through nucleophilic attack of C–F bond [64]. Although others demonstrate that  $\text{O}_2^{\bullet-}$  alone is ineffective in initiating the PFOA degradation [65], we cannot rule out the possibility that the PFOA activation via Fe complexation may favor the  $\text{O}_2^{\bullet-}$  reactivity to initiate the reaction.

To further shed light on the influence of  $\text{O}_2^{\bullet-}$ , the generation of  $\text{O}_2^{\bullet-}$  in

the catalytic system is also confirmed by EPR. Compared to the negligible background signal and TNT@AC catalysts, which are well-known as  $\text{O}_2^{\bullet-}$  producing materials [14,67], Fe-BEA150 exhibited a much stronger signal (Fig. 6C). It confirms the excellent photogeneration capacity of  $\text{O}_2^{\bullet-}$  for Fe-BEA zeolites. In addition, the PFOA photodegradation was tested in solutions bubbled with different gases ( $\text{N}_2$ ,  $\text{O}_2$ , and air) (Figure S15C). A slight decrease in defluorination ( $\sim 10\%$ ) was observed after bubbling  $\text{N}_2$ , due to the reduced dissolved oxygen in the solution and thus the  $\text{O}_2^{\bullet-}$  yield. A complete inhibition when bubbling  $\text{N}_2$ , was not observed, probably due to the strong  $\text{O}_2$  adsorption on the zeolite materials. The charge storage capacity of the materials was evaluated to estimate their  $\text{O}_2$  adsorption capacity. Cyclic voltammetry (CV) tests (Fig. 7) of BEA150,  $\text{Fe}_2\text{O}_3$ , and Fe-BEA150 were performed. The linear relationship between the scan rate and the current density difference confirms the higher double-layer capacitance ( $C_{\text{dl}}$ ) of  $\text{Fe}_2\text{O}_3$  ( $0.63$   $\text{mF cm}^{-2}$ ) compared to zeolite ( $0.48$   $\text{mF cm}^{-2}$ ) and Fe-BEA150 zeolite ( $0.60$   $\text{mF cm}^{-2}$ ).  $C_{\text{dl}}$  values indicate the electrochemical active surface area of the materials [68] and reflect the charge storage capacity which determines the affinity for electrophilic molecules such as chemisorbed  $\text{O}_2$  [69]. It is observed that the presence of Fe enhanced the electrical charge storage capacity of the pristine zeolite and therefore enhances the capacity of Fe-BEA150 to provide electrons and promote the conversion of  $\text{O}_2$  to  $\text{O}_2^{\bullet-}$  compared to the pristine zeolite, which supports the role of superoxide in the reaction system.

In fact, the electron donor properties of the  $\text{AlO}_4^-$  moieties on zeolites may favor the transition of oxygen to  $\text{O}_2^{\bullet-}$  (Eq. 8) [70] and, more importantly, stabilize  $\text{O}_2^{\bullet-}$  on its surface [71] to facilitate the reaction with PFOA. The Fe-doped BEA150 demonstrated an increased absorption spectrum in the UVA range compared with pristine BEA150 (Figure S15D), resulting in more photogenerated electrons in the conduction band (CB) to produce  $\text{O}_2^{\bullet-}$  (Eq. 9) [72].



From DFT calculations, we demonstrate a decrease in the bond dissociation energy (BDE) of the C–C bonds of PFOA (Fig. 6D) after adsorption onto the Fe-BEA zeolite. The BDE of the C1–C2 bond (see PFOA molecule in Fig. 6D) decreased from  $459$  to  $373$   $\text{kJ mol}^{-1}$ , which favors decarboxylation. These results are in agreement with a recent study, where PFOA complexed with  $\text{Fe}^{3+}$  in the solution and decreased the BDE of the C1–C2 bond to  $370.41$   $\text{kJ mol}^{-1}$  [73]. The pore-constraining effects of BEA zeolites may also impact the C–F bond energy, either through hydrophobic interaction or confinement effect in the micropores. Interestingly, the lowest bonding energy corresponds to the C5–C6 bond, the weakest point in the backbone structure of PFOA molecule [74]. After PFOA anion complexes with the Fe on zeolite surface, the carboxylate head will draw negative charge and the fluoride atoms with high electronegativity also accumulate negative charge at the hydrophobic tail, thereby tensioning the middle structure of the molecule, i.e., C5–C6. Further simulations are needed to verify these assumptions.

To summarize those results, PFOA degradation pathways are proposed. The identified short-chain PFAS (Fig. 6A) indicates a stepwise defluorination mechanism for PFOA following a decarboxylation-hydroxylation-elimination-hydrolysis (DHEH) process (Fig. 8). PFOA anions first complex with Fe on the zeolite surface and thus remain activated, as demonstrated by the reduced BDE in DFT calculations. Upon activation, UVA decarboxylation of the activated PFOA proceeds through ligand-to-metal charge transfer forming  $\bullet\text{C}_7\text{F}_{15}$  radicals that undergo stepwise defluorination [17,18]. Further hydroxylation of  $\bullet\text{C}_7\text{F}_{15}$  is carried out by  $\text{H}_2\text{O}$  to form  $\text{C}_7\text{F}_{15}\text{OH}$  that is defluorinated to  $\text{C}_7\text{F}_{13}\text{OF}$  then  $\text{C}_6\text{F}_{13}\text{COOH}$ , i.e., a stepwise defluorination. Alternatively,  $\text{O}_2^{\bullet-}$  may attack the activated carboxylic head resulting in decarboxylation and release of  $\text{F}^-$  or directly attack the C–F bond via  $\text{S}_\text{N}2$  reactions [64]. Finally, molecular oxygen and  $\text{O}_2^{\bullet-}$  can oxidize the reduced  $\text{Fe}^{2+}$  to

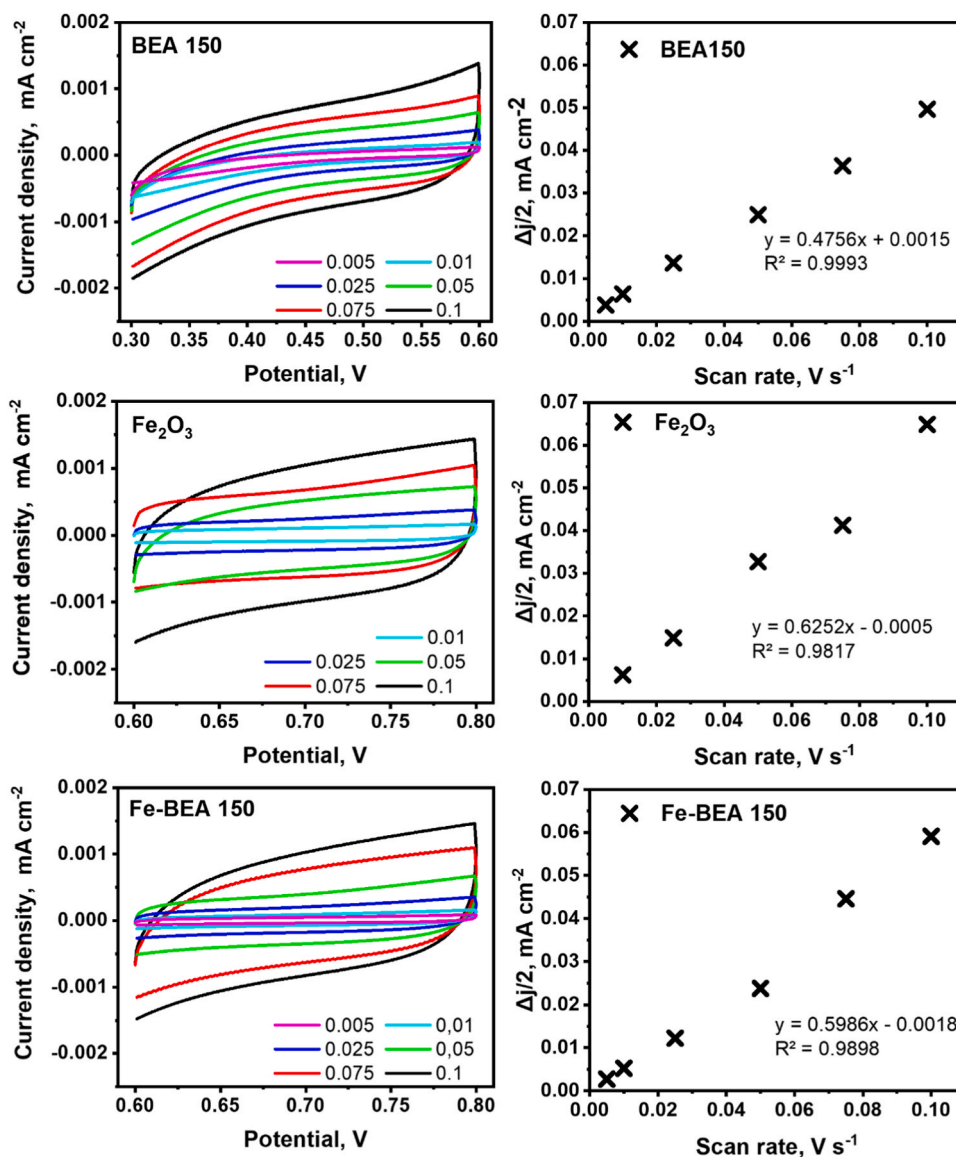


Fig. 7. Cyclic voltammetry measurements for BEA150,  $\text{Fe}_2\text{O}_3$ , and Fe-BEA150 (left); and current density difference ( $\Delta j/2$ ) as a function of the scan rate (values in the colored legend) corresponding oxygen adsorption capacity of the different materials (right).

regenerate  $\text{Fe}^{3+}$  through the Haber-Weiss mechanism [62] for continued reactions.

#### 4. Conclusions

This study investigated how to enhance the PFOA photodegradation performance of Fe-BEA zeolites by tuning the structural, textural, and composition parameters. It is proven that only pore openings comparable to PFOA molecules can efficiently capture PFOA by pore diffusion and the micropore size must be large enough for the PFOA molecules to reside. Fe doping can facilitate the complexation of PFOA via electrostatic interaction, in addition to Si-driven hydrophobic adsorption. Likewise, Fe doping has significantly increased the defluorination efficiency up to 60% in 4 hours, while an enhancement of  $\sim 20\%$  was observed with an optimized  $\text{SiO}_2/\text{Al}_2\text{O}_3$  ratio. It was found that the pH and calcination temperature were critical to stabilize the photocatalyst and minimize the leaching of the active iron sites. EPR and quenching tests demonstrated the  $\text{O}_2^-$ -driven PFOA degradation, and CV measurements confirm that  $\text{Fe}_2\text{O}_3$  may promote the  $\text{O}_2$  to  $\text{O}_2^-$  transition. DFT calculation results clarified the role of Fe in the complexation and

activation of PFOA for more effective photodegradation. This work opens new doors to tune the textural, structural, and material composition of crystalline framework materials such as zeolites, metal-organic frameworks, and covalent organic frameworks to selectively remove and degrade PFAS in waters.

#### CRediT authorship contribution statement

**Jan-Max Arana Juve:** Writing – original draft, Visualization, Validation, Methodology, Investigation, Formal analysis, Conceptualization. **Xavier Baami González:** Writing – review & editing, Methodology. **Lu Bai:** Validation, Investigation. **Zhiqun Xie:** Writing – review & editing, Validation. **Yanan Shang:** Validation, Investigation. **Ali Saad:** Writing – review & editing. **Rafael Gonzalez-Olmos:** Writing – review & editing. **Michael S. Wong:** Writing – review & editing, Supervision, Resources. **Mohamed Ateia:** Writing – review & editing, Visualization, Supervision. **Zongsu Wei:** Writing – review & editing, Visualization, Supervision, Resources, Funding acquisition, Conceptualization.

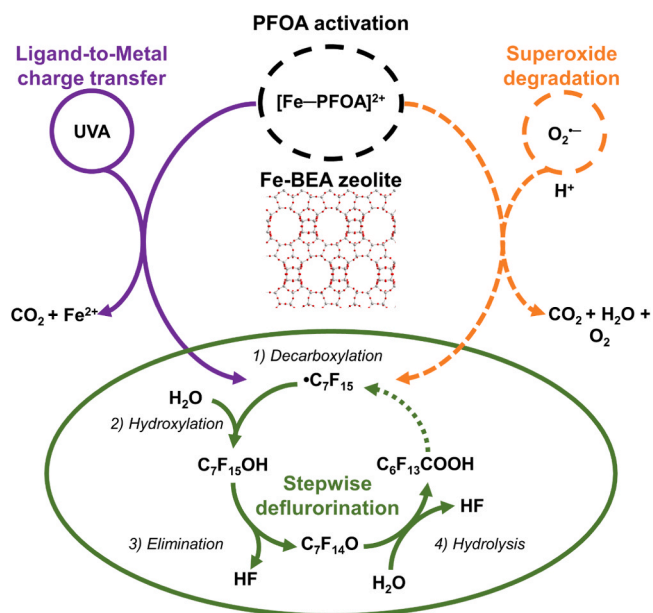


**Fig. 8.** The proposed PFOA activation mechanism through Fe complexation for stepwise DHEH defluorination via ligand-to-metal charge transfer and  $\text{O}_2^-$  under UVA initiation. Fe corresponds to the metal and PFOA corresponds to the ligand. The electron transfer occurs from the carboxylic group to  $\text{Fe}^{3+}$  in  $[\text{Fe-PFOA}]^{2+}$  [73]. The orange dotted line suggests the possible involvement of  $\text{O}_2^-$  in the defluorination process.

#### Declaration of Competing Interest

The authors declare that they have no known competing financial interests or personal relationships that could have appeared to influence the work reported in this paper.

#### Data availability

Data will be made available on request.

#### Acknowledgments

This work was supported by Aarhus University Centre for Water Technology (AU-WATEC) Start-Up Fund from Grundfos Foundation, Aarhus University Research Foundation Starting Grant (No. AUFF-E-2019-7-28), Novo Nordisk Fonden (No. NNF200C0064799), and Independent Research Fund Denmark (No. 1127-00181B and Sapere Aude Award No. 1051-00058B).

#### Appendix A. Supporting information

Supplementary data associated with this article can be found in the online version at [doi:10.1016/j.apcatb.2024.123885](https://doi.org/10.1016/j.apcatb.2024.123885).

#### References

- R.K. Singh, S. Fernando, S.F. Baygi, N. Multari, S.M. Thagard, T.M. Holsen, Breakdown products from perfluorinated alkyl substances (PFAS) degradation in a plasma-based water treatment process, *Environ. Sci. Technol.* 53 (2019) 2731–2738, <https://doi.org/10.1021/acs.est.8b07031>.
- U.S. EPA, Proposed PFAS national primary drinking water regulation, Per- and polyfluoroalkyl Subst. (2023). (<https://www.epa.gov/sdwa/and-polyfluoroalkyl-substances-pfas>) (accessed April 2, 2023).
- S.C.E. Leung, P. Shukla, D. Chen, E. Eftekhari, H. An, F. Zare, N. Ghasemi, D. Zhang, N.T. Nguyen, Q. Li, Emerging technologies for PFOS/PFOA degradation and removal: a review, *Sci. Total Environ.* 827 (2022) 153669, <https://doi.org/10.1016/j.scitotenv.2022.153669>.
- F. Li, J. Duan, S. Tian, H. Ji, Y. Zhu, Z. Wei, D. Zhao, Short-chain per- and polyfluoroalkyl substances in aquatic systems: Occurrence, impacts and treatment, *Chem. Eng. J.* 380 (2020), <https://doi.org/10.1016/j.cej.2019.122506>.
- S.P. Lenka, M. Kah, L.P. Padhye, A review of the occurrence, transformation, and removal of poly- and perfluoroalkyl substances (PFAS) in wastewater treatment plants, *Water Res.* 199 (2021) 117187, <https://doi.org/10.1016/j.watres.2021.117187>.
- W. Wang, Y. Chen, G. Li, W. Gu, T. An, Photocatalytic reductive defluorination of perfluorooctanoic acid in water under visible light irradiation: the role of electron donor, *Environ. Sci. Water Res. Technol.* 6 (2020) 1638–1648, <https://doi.org/10.1039/d0ew00205d>.
- Y. Sun, G. Li, W. Wang, W. Gu, P.K. Wong, T. An, Photocatalytic defluorination of perfluorooctanoic acid by surface defective BiOCl: Fast microwave solvothermal synthesis and photocatalytic mechanisms, *J. Environ. Sci. (China)*. 84 (2019) 69–79, <https://doi.org/10.1016/j.jes.2019.04.012>.
- J. Wang, Z. Lin, X. He, M. Song, P. Westerhoff, K. Doudrick, D. Hanigan, Critical review of thermal decomposition of Per- and polyfluoroalkyl substances: Mechanisms and implications for thermal treatment processes, *Environ. Sci. Technol.* 56 (2022) 5355–5370, <https://doi.org/10.1021/acs.est.2c02251>.
- J. Li, B.R. Pinkard, S. Wang, I.V. Novosselov, Review: hydrothermal treatment of per- and polyfluoroalkyl substances (PFAS), *Chemosphere* 307 (2022) 135888, <https://doi.org/10.1016/j.chemosphere.2022.135888>.
- D.M. Wanninayake, Comparison of currently available PFAS remediation technologies in water: a review, *J. Environ. Manag.* 283 (2021) 111977, <https://doi.org/10.1016/j.jenvman.2021.111977>.
- S. Verma, T. Lee, E. Sahle-DeMessie, M. Ateia, M.N. Nadagouda, Recent advances on PFAS degradation via thermal and nonthermal methods, *Chem. Eng. J. Adv.* 13 (2023) 100421, <https://doi.org/10.1016/j.cej.2022.100421>.
- F. Li, Z. Wei, K. He, L. Blaney, X. Cheng, T. Xu, W. Liu, D. Zhao, A concentrate-and-destroy technique for degradation of perfluorooctanoic acid in water using a new adsorptive photocatalyst, *Water Res.* 185 (2020) 1–14, <https://doi.org/10.1016/j.watres.2020.116219>.
- T. Xu, H. Ji, Y. Gu, T. Tong, Y. Xia, L. Zhang, D. Zhao, Enhanced adsorption and photocatalytic degradation of perfluorooctanoic acid in water using iron (hydr) oxides/carbon sphere composite, *Chem. Eng. J.* 388 (2020), <https://doi.org/10.1016/j.cej.2020.124230>.
- Y. Zhu, T. Xu, D. Zhao, F. Li, W. Liu, B. Wang, B. An, Adsorption and solid-phase photocatalytic degradation of perfluorooctane sulfonate in water using gallium-doped carbon-modified titanate nanotubes, *Chem. Eng. J.* 421 (2021) 129676, <https://doi.org/10.1016/j.cej.2021.129676>.
- J.M. Arana Juve, F. Li, Y. Zhu, W. Liu, L.D.M. Ottosen, D. Zhao, Z. Wei, Concentrate and degrade PFOA with a photo-regenerable composite of In-doped TNTs@AC, *Chemosphere* 300 (2022) 134495, <https://doi.org/10.1016/j.chemosphere.2022.134495>.
- J.M. Arana Juve, J.A. Donoso Reece, M.S. Wong, Z. Wei, M. Ateia, Photocatalysts for chemical-free PFOA degradation – What we know and where we go from here, *J. Hazard. Mater.* 462 (2024) 132651, <https://doi.org/10.1016/j.jhazmat.2023.132651>.
- L. Qian, F.D. Kopinke, A. Georgi, Photodegradation of perfluorooctanesulfonic acid on Fe-Zeolites in water, *Environ. Sci. Technol.* 55 (2021) 614–622, <https://doi.org/10.1021/acs.est.0c04558>.
- L. Qian, A. Georgi, R. Gonzalez-Olmos, F.D. Kopinke, Degradation of perfluorooctanoic acid adsorbed on Fe-zeolites with molecular oxygen as oxidant under UV-A irradiation, *Appl. Catal. B Environ.* 278 (2020) 119283, <https://doi.org/10.1016/j.apcatb.2020.119283>.
- M. Mancinelli, A. Martucci, L. Ahrens, Exploring the adsorption of short and long chain per- and polyfluoroalkyl substances (PFAS) to different zeolites using environmental samples, *Environ. Sci. Water Res. Technol.* (2023), <https://doi.org/10.1039/d3ew00225j>.
- S. Mitchell, A.B. Pinar, J. Kenvin, P. Crivelli, J. Kärger, J. Pérez-Ramírez, Structural analysis of hierarchically organized zeolites, *Nat. Commun.* 6 (2015), <https://doi.org/10.1038/ncomms9633>.
- F. Weinhold, R. West, Hyperconjugative interactions in permethylated siloxanes and ethers: the nature of the SiO bond, *J. Am. Chem. Soc.* 135 (2013) 5762–5767, <https://doi.org/10.1021/ja312222k>.
- S. Hossain, T.D. Stuart, B.V. Ramarao, C.C. Vanleuven, M. Wriedt, D. Kiemle, M. Satchwell, D. Kumar, Investigation into cationic surfactants and polyelectrolyte-coated  $\beta$ -zeolites for rapid and high-capacity adsorption of short- and long-chain PFAS, *Ind. Eng. Chem. Res.* 62 (2023) 8373–8384, <https://doi.org/10.1021/acs.iecr.3c00468>.
- S. Fibikar, M.T. Rinke, A. Schäfer, L. De Cola, Quantification of cation-exchanged zeolites by XPS and EDS: a comparative study, *Microporous Mesoporous Mater.* 132 (2010) 296–299, <https://doi.org/10.1016/j.micromeso.2010.02.016>.
- G.A. Bukhtiyarova, I.V. Delii, N.S. Sakaeva, V.V. Kaichev, L.M. Plyasova, V. I. Bukhtiyarov, Effect of the calcination temperature on the properties of Fe2O3/SiO2 catalysts for oxidation of hydrogen sulfide, *React. Kinet. Catal. Lett.* 92 (2007) 89–97, <https://doi.org/10.1007/s11144-007-5177-2>.
- L. Duan, B. Wang, K.N. Heck, C.A. Clark, J. Wei, M. Wang, J. Metz, G. Wu, A. L. Tsai, S. Guo, J. Arredondo, A.D. Mohite, T.P. Senfite, P. Westerhoff, P. Alvarez, X. Wen, Y. Song, M.S. Wong, Titanium oxide improves boron nitride photocatalytic degradation of perfluorooctanoic acid, *Chem. Eng. J.* 448 (2022) 137735, <https://doi.org/10.1016/j.cej.2022.137735>.
- L. Sun, J.R. Bolton, Determination of the quantum yield for the photochemical generation of hydroxyl radicals in TiO<sub>2</sub> suspensions, *J. Phys. Chem.* 100 (1996) 4127–4134, <https://doi.org/10.1021/jp9505800>.
- L. Duan, B. Wang, K. Heck, S. Guo, C.A. Clark, J. Arredondo, M. Wang, T.P. Senfite, P. Westerhoff, X. Wen, Y. Song, M.S. Wong, Efficient photocatalytic PFOA degradation over boron nitride, *Environ. Sci. Technol. Lett.* 7 (2020) 613–619, <https://doi.org/10.1021/acs.estlett.0c00434>.

- [28] M.J. Frisch, G.W. Trucks, H.B. Schlegel, G.E. Scuseria, M.A. Robb, J.R. Cheeseman, G. Scalmani, V. Barone, B. Mennucci, G.A. Petersson, H. Nakatsuji, M. Caricato, X. Li, H.P. Hratchian, A.F. Izmaylov, J. Bloino, G. Zheng, J.L. Sonnenberg, M. Hada, M. Ehara, K. Toyota, R. Fukuda, J. Hasegawa, M. Ishida, T. Nakajima, Y. Honda, O. Kitao, H. Nakai, T. Vreven, J.A. Montgomery, J.E. Peralta, F. Ogliaro, M. Bearpark, J.J. Heyd, E. Brothers, K.N. Kudin, V.N. Staroverov, R. Kobayashi, J. Normand, K. Raghavachari, A. Rendell, J.C. Burant, S.S. Iyengar, J. Tomasi, M. Cossi, N. Rega, J.M. Millam, M. Klene, J.E. Knox, J.B. Cross, V. Bakken, C. Adamo, J. Jaramillo, R. Gomperts, R.E. Stratmann, O. Yazyev, A.J. Austin, R. Cammi, C. Pomelli, J.W. Ochterski, R.L. Martin, K. Morokuma, V.G. Zakrzewski, G.A. Voth, P. Salvador, J.J. Dannenberg, S. Dapprich, A.D. Daniels, Farkas, J. B. Foresman, J.V. Ortiz, J. Cioslowski, D.J. Fox, Gaussian 09, Revision D.01, Gaussian, Inc., Wallingford CT, 2013, pp. 1–20.
- [29] T. Lu, F. Chen, Multiwfn: a multifunctional wavefunction analyzer, *J. Comput. Chem.* 33 (2012) 580–592, <https://doi.org/10.1002/jcc.22885>.
- [30] W. Humphrey, A. Dalke, K. Schulten, VMD: visual molecular dynamics, *J. Mol. Graph.* 14 (1996) 33–38, [https://doi.org/10.1016/0263-7855\(96\)00018-5](https://doi.org/10.1016/0263-7855(96)00018-5).
- [31] J. Liu, D.J. Van Hoornissen, T. Liu, A. Maizel, X. Huo, S.R. Fernández, C. Ren, X. Xiao, Y. Fang, C.E. Schaefer, C.P. Higgins, S. Vyas, T.J. Strathmann, Reductive defluorination of branched per- and polyfluoroalkyl substances with cobalt complex catalysts, *Environ. Sci. Technol. Lett.* 5 (2018) 289–294, <https://doi.org/10.1021/acs.estlett.8b00122>.
- [32] T.D. Courtney, C.C. Chang, R.J. Gorte, R.F. Lobo, W. Fan, V. Nikolakis, Effect of water treatment on Sn-BEA zeolite: origin of 960 cm<sup>-1</sup> FTIR peak, *Microporous Mesoporous Mater.* 210 (2015) 69–76, <https://doi.org/10.1016/j.micromeso.2015.02.012>.
- [33] J.L. Hodala, A.B. Halgeri, G.V. Shanbhag, Enhancement in activity and shape selectivity of zeolite BEA by phosphate treatment for 2-methoxynaphthalene acylation, *RSC Adv.* 6 (2016) 90579–90586, <https://doi.org/10.1039/c6ra16093j>.
- [34] D.P. Serrano, J.M. Escola, P. Pizarro, Synthesis strategies in the search for hierarchical zeolites, *Chem. Soc. Rev.* 42 (2013) 4004–4035, <https://doi.org/10.1039/c2cs35330j>.
- [35] L.B. McCusker, D.H. Olson, C. Baerlocher Atlas Zeolite Framew. Types ,2007, 10.1016/B978-0-444-53064-6.X5186-X.
- [36] K. Miyake, R. Inoue, T. Miura, M. Nakai, H. Al-Jabri, Y. Hirota, Y. Uchida, S. Tanaka, M. Miyamoto, S. Inagaki, Y. Kubota, C.Y. Kong, N. Nishiyama, Improving hydrothermal stability of acid sites in MFI type aluminosilicate zeolite (ZSM-5) by coating MFI type all silica zeolite (silicalite-1) shell layer, *Microporous Mesoporous Mater.* 288 (2019) 109523, <https://doi.org/10.1016/j.micromeso.2019.05.048>.
- [37] N. Katada, H. Igi, J.H. Kim, M. Niwa, Determination of the acidic properties of zeolite by theoretical analysis of temperature-programmed desorption of ammonia based on adsorption equilibrium, *J. Phys. Chem. B.* 101 (1997) 5969–5977, <https://doi.org/10.1021/jp9639152>.
- [38] M. Ravi, V.L. Sushkevich, J.A. van Bokhoven, On the location of Lewis acidic aluminum in zeolite mordenite and the role of framework-associated aluminum in mediating the switch between Brønsted and Lewis acidity, *Chem. Sci.* 12 (2021) 4094–4103, <https://doi.org/10.1039/d0sc06130a>.
- [39] M. Ravi, V.L. Sushkevich, J.A. van Bokhoven, Towards a better understanding of Lewis acidic aluminium in zeolites, *Nat. Mater.* 19 (2020) 1047–1056, <https://doi.org/10.1038/s41563-020-0751-3>.
- [40] D.L. Bish, F. Blake, T. Vaniman, J. Chipera, V. Morris, W. Ming, H. Treiman, P. Sarrazin, S.M. Morrison, T. Downs, N. Achilles, S. Yen, F. Bristow, A. Crisp, M. Morozkian, J.D. Farmer, E.B. Ramp, M.S. Team, X-ray diffraction results from marsscience laboratory: mineralogy of rocknest at teal crater, *Science* 341 (2013) 1238932, <https://doi.org/10.1126/science.1238932>.
- [41] S.S.U. Rahman, M.T. Qureshi, K. Sultana, W. Rehman, M.Y. Khan, M.H. Asif, M. Farooq, N. Sultana, Single step growth of iron oxide nanoparticles and their use as glucose biosensor, *Results Phys.* 7 (2017) 4451–4456, <https://doi.org/10.1016/j.rinp.2017.11.001>.
- [42] M. Van den Bergh, A. Krajnc, S. Voorspoels, S.R. Tavares, S. Mullens, I. Beurroies, G. Maurin, G. Mali, D.E. De Vos, Highly selective removal of perfluorinated contaminants by adsorption on all-silica zeolite beta, *Angew. Chem.* 132 (2020) 14190–14194, <https://doi.org/10.1002/ange.202002953>.
- [43] S. Kalam, S.A. Abu-Khamsin, M.S. Kamal, S. Patil, Surfactant adsorption isotherms: a review, *ACS Omega* 6 (2021) 32342–32348, <https://doi.org/10.1021/acsomega.1c04661>.
- [44] J. Xu, Z. Liu, D. Zhao, N. Gao, X. Fu, Enhanced adsorption of perfluorooctanoic acid (PFOA) from water by granular activated carbon supported magnetite nanoparticles, *Sci. Total Environ.* 723 (2020) 137757, <https://doi.org/10.1016/j.scitotenv.2020.137757>.
- [45] U. Shafique, V. Dorn, A. Paschke, G. Schüürmann, Adsorption of perfluorocarboxylic acids at the silica surface, *Chem. Commun.* 53 (2017) 589–592, <https://doi.org/10.1039/c6cc07525h>.
- [46] M. Fugel, M.F. Hesse, R. Pal, J. Beckmann, D. Jayatilaka, M.J. Turner, A. Karton, P. Bultinck, G.S. Chandler, S. Grabowsky, Covalency and ionicity do not oppose each other—relationship between Si–O bond character and basicity of siloxanes, *Chem. - A Eur. J.* 24 (2018) 15275–15286, <https://doi.org/10.1002/chem.201802197>.
- [47] M. Moshoeshoe, M. Silas Nadiye-Tabbiruka, V. Obuseng, A review of the chemistry, structure, properties and applications of zeolites, *Am. J. Mater. Sci.* 2017 (2017) 196–221, <https://doi.org/10.5923/j.materials.20170705.12>.
- [48] K.-U. Goss, The pKa values of PFOA and other highly fluorinated carboxylic acids, 5032–5032, *Environ. Sci. Technol.* 42 (2008), <https://doi.org/10.1021/es8011904>.
- [49] J.M. Arana Juve, B. Wang, M.S. Wong, M. Ateia, Z. Wei, Complete defluorination of per- and polyfluoroalkyl substances — dream or reality? *Curr. Opin. Chem. Eng.* 41 (2023) 100943 <https://doi.org/10.1016/j.coch.2023.100943>.
- [50] P. Bhavani, N.R. Reddy, I.V.S. Reddy, M. Sakar, Manipulation over phase transformation in iron oxide nanoparticles via calcination temperature and their effect on magnetic and dielectric properties, *IEEE Trans. Magn.* 53 (2017) 18–22, <https://doi.org/10.1109/TMAG.2017.2715320>.
- [51] C.J. Heard, L. Grajciar, F. Uhlík, M. Shamzhy, M. Opanasenko, J. Čejka, P. Nachtigall, Zeolite (In)Stability under aqueous or steaming conditions, *Adv. Mater.* 32 (2020), <https://doi.org/10.1002/adma.202003264>.
- [52] D.G. Fatouros, D. Douroumis, V. Nikolakis, S. Ntais, A.M. Moschovi, V. Trivedi, B. Khima, M. Roldo, H. Nazar, P.A. Cox, In vitro and in silico investigations of drug delivery via zeolite BEA, *J. Mater. Chem.* 21 (2011) 7789–7794, <https://doi.org/10.1039/c1jm10204d>.
- [53] J.M. Arana Juve, F.M.S. Christensen, Y. Wang, Z. Wei, Electrodialysis for metal removal and recovery: a review, *Chem. Eng. J.* 435 (2022) 134857, <https://doi.org/10.1016/j.cej.2022.134857>.
- [54] X. Wang, W. Wang, Y. Liu, M. Ren, H. Xiao, X. Liu, Characterization of conformation and locations of C-F Bonds in graphene derivative by polarized ATR-FTIR, *Anal. Chem.* 88 (2016) 3926–3934, <https://doi.org/10.1021/acs.analchem.6b00115>.
- [55] Y.H. Kim, M.S. Hwang, H.J. Kim, J.Y. Kim, Y. Lee, Infrared spectroscopy study of low-dielectric-constant fluorine-incorporated and carbon-incorporated silicon oxide films, *J. Appl. Phys.* 90 (2001) 3367–3370, <https://doi.org/10.1063/1.1402152>.
- [56] S.S. Yi, B.R. Wulan, J.M. Yan, Q. Jiang, Highly efficient photoelectrochemical water splitting: Surface modification of cobalt-phosphate-loaded Co<sub>3</sub>O<sub>4</sub>/Fe<sub>2</sub>O<sub>3</sub> p-n heterojunction nanorod arrays, *Adv. Funct. Mater.* 29 (2019) 1–9, <https://doi.org/10.1002/adfm.201801902>.
- [57] N. Wang, L. Zhu, D. Wang, M. Wang, Z. Lin, H. Tang, Sono-assisted preparation of highly-efficient peroxidase-like Fe<sub>3</sub>O<sub>4</sub> magnetic nanoparticles for catalytic removal of organic pollutants with H<sub>2</sub>O<sub>2</sub>, *Ultrason. Sonochem.* 17 (2010) 526–533, <https://doi.org/10.1016/j.ultsonch.2009.11.001>.
- [58] T. Ikuno, W. Chaikittisilp, Z. Liu, T. Iida, Y. Yanaba, T. Yoshikawa, S. Kohara, T. Wakihara, T. Okubo, Structure-directing behaviors of tetraethylammonium cations toward zeolite beta revealed by the evolution of aluminosilicate species formed during the crystallization process, *J. Am. Chem. Soc.* 137 (2015) 14533–14544, <https://doi.org/10.1021/jacs.5b11046>.
- [59] Y. Du, Z. Huang, J. Zhang, G. Jing, Fe<sub>2</sub>O<sub>3</sub>/HY Catalyst: a microporous material with zeolite-type framework achieving highly improved alkali poisoning-resistant performance for selective reduction of NOx with NH<sub>3</sub>, *Environ. Sci. Technol.* 54 (2020) 7078–7087, <https://doi.org/10.1021/acs.est.0c00298>.
- [60] Z. Song, X. Dong, N. Wang, L. Zhu, Z. Luo, J. Fang, C. Xiong, Efficient photocatalytic defluorination of perfluorooctanoic acid over BiOCl nanosheets via a hole direct oxidation mechanism, *Chem. Eng. J.* 317 (2017) 925–934, <https://doi.org/10.1016/j.cej.2017.02.126>.
- [61] Z. Song, X. Dong, J. Fang, C. Xiong, N. Wang, X. Tang, Improved photocatalytic degradation of perfluorooctanoic acid on oxygen vacancies-tunable bismuth oxychloride nanosheets prepared by a facile hydrolysis, *J. Hazard. Mater.* 377 (2019) 371–380, <https://doi.org/10.1016/j.jhazmat.2019.05.084>.
- [62] A.G. Gonzalez, J.M. Santana-Casiano, N. Perez, M. Gonzalez-Davila, Oxidation of Fe(II) in natural waters at high nutrient concentrations, *Environ. Sci. Technol.* 44 (2010) 8095–8101, <https://doi.org/10.1021/es1009218>.
- [63] J. Wang, C. Cao, Y. Zhang, Y. Zhang, L. Zhu, Underneath mechanisms into the super effective degradation of PFOA by BiOF nanosheets with tunable oxygen vacancies on exposed (101) facets, *Appl. Catal. B Environ.* 286 (2021) 119911, <https://doi.org/10.1016/j.apcatb.2021.119911>.
- [64] L. Bai, Y. Jiang, D. Xia, Z. Wei, R. Spinney, D.D. Dionysiou, D. Minakata, R. Xiao, H. Bin Xie, L. Chai, Mechanistic understanding of superoxide radical-mediated degradation of perfluorocarboxylic acids, *Environ. Sci. Technol.* 56 (2022) 624–633, <https://doi.org/10.1021/acs.est.1c06356>.
- [65] H. Javed, J. Metz, T.C. Eraslan, J. Mathieu, B. Wang, G. Wu, A. Tsai, M.S. Wong, P. J.J. Alvarez, Discerning the relevance of superoxide in PFOA degradation, *Environ. Sci. Technol. Lett.* 7 (2020) 653–658, <https://doi.org/10.1021/acs.estlett.0c00505>.
- [66] J. Liu, X. Zhang, Q. Zhong, J. Li, H. Wu, B. Zhang, L. Jin, H.B. Tao, B. Liu, Electrostatic self-assembly of a AgI/Bi<sub>2</sub>Ga<sub>4</sub>O<sub>9</sub> p-n junction photocatalyst for boosting superoxide radical generation, *J. Mater. Chem. A* 8 (2020) 4083–4090, <https://doi.org/10.1039/c9ta13724f>.
- [67] Q. Wang, X. Lei, F. Pan, D. Xia, Y. Shang, W. Sun, W. Liu, A new type of activated carbon fibre supported titanate nanotubes for high-capacity adsorption and degradation of methylene blue, *Colloids Surf. A Physicochem. Eng. Asp.* 555 (2018) 605–614, <https://doi.org/10.1016/j.colsurfa.2018.07.016>.
- [68] Y. Lyu, J. Zheng, Z. Xiao, S. Zhao, S.P. Jiang, S. Wang, Identifying the intrinsic relationship between the restructured oxide layer and oxygen evolution reaction performance on the cobalt pnictide catalyst, *Small* 16 (2020) 1–8, <https://doi.org/10.1002/smll.201906867>.
- [69] M. Mishra, D.M. Chun, α-Fe<sub>2</sub>O<sub>3</sub> as a photocatalytic material: a review, *Appl. Catal. A Gen.* 498 (2015) 126–141, <https://doi.org/10.1016/j.apcata.2015.03.023>.
- [70] T. Crémoux, I. Batonneau-Gener, A. Moissette, J.L. Paillaud, M. Hureau, E. Ligner, C. Morais, S. Laforge, C. Marichal, H. Nouali, Influence of framework Si/Al ratio and topology on electron transfers in zeolites, *Phys. Chem. Chem. Phys.* 21 (2019) 14892–14903, <https://doi.org/10.1039/c9cp01166h>.
- [71] K.B. Yoon, Electron- and charge-transfer reactions within zeolites, *Chem. Rev.* 93 (1993) 321–339, <https://doi.org/10.1021/cr00017a015>.

- [72] M. Mishra, D.M. Chun,  $\alpha$ -Fe<sub>2</sub>O<sub>3</sub> as a photocatalytic material: a review, *Appl. Catal. A Gen.* 498 (2015) 126–141, <https://doi.org/10.1016/j.apcata.2015.03.023>.
- [73] Y. Chen, H. Ma, J. Zhu, Y. Gu, T. Liu, New insights into ferric iron-facilitated UV254 photolytic defluorination of perfluorooctanoic acid (PFOA): combined experimental and theoretical study, *J. Hazard. Mater.* 434 (2022) 128865, <https://doi.org/10.1016/j.jhazmat.2022.128865>.
- [74] Y. Chen, H. Ma, J. Zhu, Y. Gu, T. Liu, New insights into ferric iron-facilitated UV254 photolytic defluorination of perfluorooctanoic acid (PFOA): combined experimental and theoretical study, *J. Hazard. Mater.* 434 (2022), <https://doi.org/10.1016/j.jhazmat.2022.128865>.
- [75] M. Khaleel, J.M. Arana Juve, S. Khalil, A. Elmhamdi, Intergrowth of zeolites LTA and FAU/EMT in nanosized particles synthesized from organic-free gels, *Cryst. Growth Des.* 23 (5) (2023) 3104–3112, <https://doi.org/10.1021/acs.cgd.2c01008>.